PHYSICAL REVIEW A VOLUME 36, NUMBER 12 DECEMBER 15, 1987

Experimental and theoretical investigations of the optogalvanic effect in a Hg-Ar discharge

W. H. Richardson* and L. Maleki†
Jet Propulsion Laboratory, California Institute of Technology, 4800 Oak Grove Drive, Pasadena, California 91109

E. Garmire
Center for Laser Studies, University of Southern California, University Park, Los Angeles, CA 90089-1112
(Received 15 May 1987)

The optogalvanic effect induced in a Hg-Ar discharge by light at 546.1 nm is studied experimentally and theoretically. The plasma and its response to a disturbance in the atomic-level populations are described entirely in terms of electron collision cross sections and other fundamental parameters. In a detailed description of the laser interaction with the atomic system, it was necessary to take into account velocity-changing collisions (VCC). These collisions (VCC) strongly modify the interaction between the Doppler-broadened system and the optical field. In some Doppler-free optogalvanic spectra the dramatic influence of VCC on the velocity distribution of atomic-level population is evident. Measurements of the magnitude of the optogalvanic signal confirm most of the theoretical results. Some anomalous features of the impedance change due to a weak beam were observed when a strong counterpropagating beam was introduced.

I. INTRODUCTION

The optogalvanic effect (OGE) is the change in the electrical properties of a discharge that occurs when the medium absorbs radiation. The effect has been utilized for spectroscopy[1] and discharge diagnostics.[2,3]

Theoretical predictions of the magnitude of the effect and its dependence on discharge parameters have been meager compared with experimental observations. Pepper[4] and Maeda *et al.*[5] have studied the effect in a Na–rare-gas discharge. Lawler[6] has developed a model based on perturbation of the rate equations rather than a direct solution of those equations. That approach is especially useful in cases where many of the collision cross sections are not known. Since in that model the discharge response to an electrical disturbance is parametrized by an empirical quantity termed the dynamic resistance. His model, the first to be compared with experiments, agrees with measurements performed in the positive columns of helium and neon discharges.[6]

In this paper the OGE induced in a Hg-Ar discharge by light at 546.1 nm (corresponding to the 6^3P_2-7^3S_1 mercury transition) is studied experimentally and theoretically. We have utilized the OGE for spectroscopy of levels in Hg and Hg^+ and for diagnostics of Hg-Ar discharges that may serve as an incoherent optical source at 194 nm. Those studies were supportive of efforts to develop a frequency standard based on trapped mercury ions[7] and were the original motivation for inquiry into the optogalvanic effect. In the course of that work, it became clear that the Hg-Ar discharge is one of the best systems for investigating the mechanisms responsible for the OGE. This is because it is one of the best characterized gaseous plasmas. A study of the OGE would assist discharge diagnostics as well as the development of an opening switch that may be based on this effect.[8] Additionally, such a study, along with an understanding of the particular effects of the laser-plasma interaction on the transmitted beams, is directly applicable to the optical diagnostics of fluorescence lamps. Finally, in the type of discharge in which one of the earliest observations of the OGE was recorded,[9] it is now possible to predict for the first time the magnitude of the effect.

The theoretical segment of the study is based entirely on fundamental parameters (cross sections, energy distribution for the electrons, etc). Because of the technological importance[10,11] of Hg-vapor discharges, accurate data on cross sections, electron mobilities, and other parameters necessary for modeling the laser-discharge interaction are available in the literature. The predicted change in discharge current, ΔI_D, with laser power agrees with the measured values for over three decades of input optical power, while deviations occur at the highest input powers (>90 mW). In particular, ΔI_D does not saturate as the population difference saturates. The population difference was obtained from measurements of the optical absorption. Additionally, the intensity-dependent absorption saturates as if the transition were homogeneously broadened. This unexpected behavior for a low-pressure discharge with Doppler broadening is attributed to cross relaxation. Cross relaxation, in this case due to velocity-changing collisions (VCC), modifies the interaction between the atoms and optical field. The effects of velocity-changing collisions were included in the model.

The presence of VCC were also observed in some Doppler-free optogalvanic spectra. In those spectra we have observed that a single beam can saturate the transition for all velocity groups because of cross relaxation. Measurements of ΔI_D versus discharge current with a fixed input optical power agree with the predicted values only over a limited range of current densities. Finally, we have observed, for the first time, optogalvanic Lamb

dips that extend below the dark impedance, indicating a reversal of the steady-state impedance change on resonance.

This paper is structured as follows. The mechanisms responsible for the optogalvanic effect are discussed in Sec. II A. In Sec. II B a rate-equation description of the plasma and laser interaction with the level populations is presented. The solution of the equations is discussed in Sec. II C. A description of the equipment and experimental arrangement follows, Sec. III. A discussion of the experimental results and comparison between experimental values and estimates for some parameters is given in Sec. IV. Our results in optogalvanic spectroscopy follows (Sec. V) and then there is a summary and three appendixes.

II. THEORY

A. Physical description of the effect

The optogalvanic effect is due to the following processes: (i) a redistribution of the population among levels having different ionization rates and (ii) a change in the electron temperature.

A partial energy diagram for neutral Hg is shown in Fig. 1. The induced OGE is due almost entirely to the depletion of the $^3P_2$ metastable level. Significant depletion occurs because the 7^3S_1 level is radiatively coupled to the $^3P_1$ level, which returns most of the atoms to the ground state. Removal of atoms from the 6^3P_2 level that can participate in the two-step excitation, through the $^3P_2$ level, leads to a decrease in the density of electrons and ions generated. In the low-pressure and low-current-density discharges of the type employed in this study, two-step ionization through the ^3P levels is the dominant ionization route.[12] A decrease in the discharge current in the presence of 546.1-nm light has been measured. This is a negative OGE.[6] Depletion of the metastable population also reduces the contribution of the corresponding level to the total ionization rate. To restore equality between the total electron-generation rate and electron-loss rate, the electron temperature increases. The electron-loss rate is independent of the optical field and determined mainly by the electron diffusion constant and cell diameter.

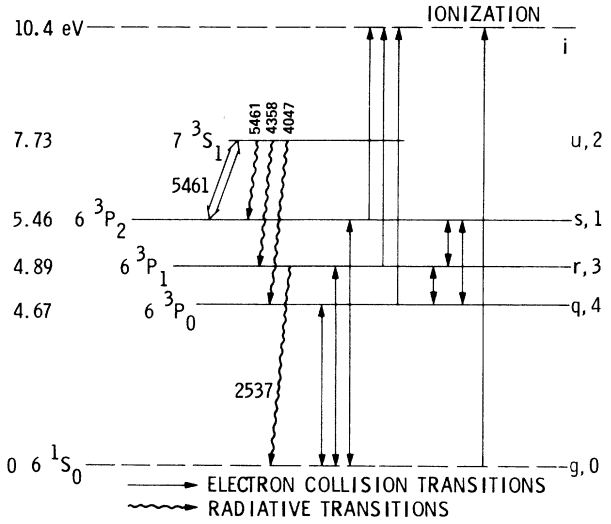

FIG. 1. Partial energy diagram of Hg. Included are the dominant transitions due to electron-atom collisions and the laser field at 5461 Å.

B. Rate equations for the plasma and laser interaction with the atomic system

This model describes the change in the electrical properties of the positive column of a Hg-Ar discharge when an optical field at 546.1 nm is applied. Models of the optogalvanic effect are necessarily discharge specific. However, our approach is generally applicable whenever a Maxwell-Boltzmann function adequately describes the electron-energy distribution and the radiation interacts with excited levels.

Equations (1)–(7) describe the Hg-Ar discharge coupled to the laser field and Eq. (8) is a constraint provided by the circuit. The level populations are labeled as n_j ($j=q,r,s,u$). If the optical field is removed, the model is representative of those typically employed for Hg-Ar discharges,[10,11]

$$\frac{\partial n_s}{\partial t}=n_e[k_{gs}n_g+k_{qs}n_q+k_{rs}n_r -(k_{sg}+k_{sq}+k_{sr})n_s-k_{si}n_s] -\frac{\sigma(\nu)I_\nu}{h\nu}\left[n_s-\frac{g_s}{g_u}n_u\right]+n_u/\tau_{us} , \tag{1}$$

$$\frac{\partial n_u}{\partial t}=\frac{\sigma(\nu)I_\nu}{h\nu}\left[n_s-\frac{g_s}{g_u}n_u\right]-n_u/\tau_u , \tag{2}$$

$$\frac{\partial n_q}{\partial t}=n_e[k_{gq}n_g+k_{rq}n_r+k_{sq}n_s -(k_{qg}+k_{qr}+k_{qs})n_q-k_{qi}n_q]+n_u/\tau_{uq} , \tag{3}$$

$$\frac{\partial n_r}{\partial t}=n_e[k_{gr}n_g+k_{qr}n_q+k_{sr}n_s -(k_{rg}+k_{rq}+k_{rs})n_r-k_{ri}n_r] -n_r/\tau_r+n_u/\tau_{ur} , \tag{4}$$

$$\frac{\partial n_e}{\partial t}=D_a\nabla^2 n_e+n_e(k_{gi}n_g+k_{qi}n_q+k_{ri}n_r+k_{si}n_s) , \tag{5}$$

$$n_e\frac{\partial U_e}{\partial t}=n_e\left[-\chi\nu_{\rm col}(U_e-U_g)+q\mu_e E^2 -\sum_{x,y}k_{xy}n_x\Delta U_{xy}\right] , \tag{6}$$

$$J=n_e e\mu_e E , \tag{7}$$

$$Z\,\Delta I_D + L\,\Delta E = 0 \ . \tag{8}$$

A list of the parameters used in these equations and elsewhere in this paper is given in Appendix A. Some of the parameters are known and available in the literature. Others are calculated from the theory of plasmas. The quantities in Eqs. (1)–(7) are defined in the following paragraphs. The rate coefficients for electron-atom collisions are given by[12,13]

$$k_{xy} = \int_0^\infty v_e f(\varepsilon)\sigma_{xy}(\varepsilon)d\varepsilon \ ,$$

where $v_e = (2\varepsilon/m)^{1/2}$ is the electron thermal speed, $f(\varepsilon)$ the electron energy distribution, and σ_{xy} the collision cross section for the atom transition from level x to y. Assuming a maxwellian electron-energy distribution, and for upward-transitions cross sections linear in electron energy above the excitation threshold, we obtain

$$k_{xy} = \left[\frac{2^3}{\pi m}\right]^{1/2} \sigma^0_{xy}(kT_e)^{1/2}(\varepsilon_{xy} + 2kT_e)e^{-\varepsilon_{xy}/kT_e} \ ,$$

where $\varepsilon_{xy} = \varepsilon_y - \varepsilon_x \geq 0$ and ε_j is the energy of level j.

The rate coefficients for downward transitions, that is electron-atom collisions of the second kind (or superelastic collisions), are obtained from detailed balancing,[14]

$$k_{xy} = \frac{g_y}{g_x}\left[\frac{2^3}{\pi m}\right]^{1/2} \sigma^0_{xy}(kT_e)^{1/2}(\varepsilon_{xy} + 2kT_e) \ , \quad \varepsilon_x > \varepsilon_y$$

Other quantities in Eqs. (1)–(7) are the electron-argon collision frequency $\nu_{\rm col}$, ambipolar diffusion coefficient D_a, electron mobility μ_e, and the fractional energy loss per electron per elastic collision χ. These obey the following equations:[11]

$$\nu_{\rm col} = \nu_0^* p_{\rm Ar}(kT_e/e)^{1.65} \ ,$$

$$D_a = \mu_{\rm ion}(kT_e/e + kT_i/e) \ ,$$

$$\mu_e = \mu_e^* p_{\rm Ar}^{-1}(kT_e/e)^{-1.65} \ ,$$

$$\chi = 2m/M_{\rm Ar} = 2.7\times 10^{-5} \ ,$$

where ν_0^*, $u_{\rm ion}$, μ_e^*, and σ^0_{xy} are obtained from Polman[11] [the cross sections (σ^0_{xy}) were used without the suggested corrections]. Also I_ν is the intensity of the laser at frequency ν, E is the electric field in the positive column, Z is the circuit impedance in series with the discharge, g_j is the degeneracy of level j, $\tau_{uj} = 1/\gamma_{uj}$ where γ_{uj} is the transition probability from level u to j, and $\sigma(\nu)$ is the optical absorption cross section;[13] $\sigma(\nu) = \gamma_{us}c^2 g_u/(\nu^2 8\pi g_s)g(\nu)$, where $g(\nu)$ is the line-shape function. Also U_e is the electron energy, U_g is the average thermal energy of an argon atom, and $U_{xy} = U_y - U_x$ is the energy difference between level x and y. In the energy-balance equation (6), the summation is over all transitions ($x = g,q,r,s$ and $y = g,q,r,s,i$). If the transition is to the ionized state then wall losses are included by taking $\Delta U_{xy} = U_y - U_x + 5kT_e/2$.

Radiation trapping is included in the radiative lifetime τ_r of level r, $\tau_r = \tau_r'/g_{tr}$ where[15] τ_r' is the natural radiative lifetime and $g_{tr} = 1.6\times 5/\{k_0 R[\pi \ln(k_0 R/5)]^{1/2}\}$ and $k_0 = 4.6\times 10^{-13} n_g$; n_g is the ground-state density. The factor 5 in g_{tr} stems from the assumption that natural mercury has approximately five equally abundant isotopes.

C. Solution of the equations

1. *Absence of the laser*

The system of equations is numerically solved first with the laser power P_L equal to zero and n_u negligible compared to the other populations. Then the optical field is added. The spatial dependence implicitly included in the above equations is removed by averaging the particle densities over the cell radius $R = 1.3$ cm. The excited-state densities are assumed to be best described by a parabolic function[12] $n_j(\rho) = n_j(0)(1-\rho^2/R^2)$ $j = q,r,s$ and ρ is the polar radial coordinate. Also the electron density is described by the zeroth-order Bessel function, $n_e(\rho) = n_e(0)J_0(2.4\rho/R)$. Spatially averaging the particle densities and assuming steady-state conditions, Eqs. (1), (3), and (4) then reduce to three simultaneous linear equations that determine the population densities. A transcendental equation, obtained from the ionization-balancing equation (5), determines the electron temperature. Equation (6) yields the electric field in terms of the electron temperature and population densities. An iterative procedure is used to determine the unperturbed discharge ($P_L = 0$) conditions (T_e^0, n_e^0, n_j^0, and E^0) in terms of the current (I_D), mercury pressure ($p_{\rm Hg}$), and argon pressure ($p_{\rm Ar}$). A flowchart of the computation process is given in Appendix B.

An initial guess at T_e^0 and n_e^0 allows computation of the rate coefficients. The simultaneous linear equations for n_j are then solved to give $n_j^{0\prime}$. Substituting $n_j^{0\prime}$ into the ionization-balance equation gives, via a root-finding procedure, an improved estimate for the electron temperature, $T_e^{0\prime}$. The new value $T_e^{0\prime}$ is checked against the previous T_e^0 and if they agree to within specified limits computation proceeds to the next step. Otherwise $T_e^{0\prime}$ is incremented and $n_j^{0\prime}$ is recomputed; and this segment of the computation is repeated until an electron temperature that gives the correct population, and vice versa, is found. Substituting the appropriate T_e^0 and n_j^0 in the energy-balance equation yields the electric field E^0. The electron density is then computed for the specified current. If n_e^0 and E^0 agree with previous values to within specified limits, the computation process terminates. Otherwise n_e^0 is incremented, and n_j^0 and then T_e^0 are recomputed until the process converges. Convergence is swift, generally requiring no more than four complete loop iterations to obtain n_e^0 and E^0 to within 10% of final values. The accuracy to within which T_e^0 and E^0 must be computed is determined by the precision to which the change in discharge voltage must be predicted. To predict $|\Delta V_D|$ to within 0.1 mV requires that E be computed to within 10^{-3} V/m and $|\Delta T_e^0|/T_e < 10^{-6}$.

2. *Optical field added*

In moderate to intense discharges ($n_e > 10^{11}$ cm^3) the optical field perturbs the populations by no more than a

few percent. Hence to first order the change in populations δn_j is unaffected by the optically induced change in the rates. Using this fact, an analytical solution for the optically induced change in the population densities is possible. Before proceeding to solve (1)–(7), an additional effect must be taken into account. VCC modify the interaction between the monochromatic beam and the Doppler-broadened multilevel system.[16–18] The effects of VCC on atomic-level populations can be explained by referring to Fig. 2. In the absence of VCC, a monochromatic beam interacts only with atoms of a particular velocity group. The velocity group centered at $v=(\omega_0-\omega)/k$ (ω_0 is the atomic transition frequency and ω is the laser frequency) is Doppler shifted into resonance with the beam. In the presence of VCC, atoms from other velocity groups can be brought into resonance with the laser. In this way the laser interacts with the entire Doppler profile. Velocity-changing collisions are due mainly to collisions between mercury and argon atoms. The principal effect of VCC is to increase the saturation intensity and modify the saturation behavior from an inhomogeneously broadened line towards a homogeneously broadened line. These collisions also modify the nonlinear optical properties of the two-level system.[18]

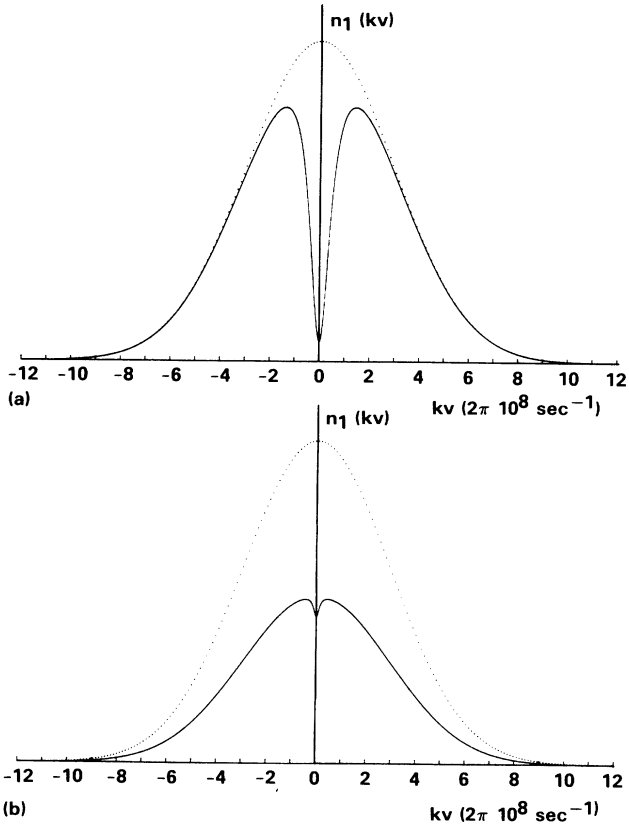

FIG. 2. Effects of velocity-changing collisions on the velocity distribution of atomic level populations. Dotted curve is the population with zero input optical power. (a) Absence of VCC. (b) Atoms undergo VCC. Graphs were calculated assuming $\Delta\nu_D=700$ MHz, $\Gamma_{vcc}=5\times10^6$ sec^{-1}, and $I_{in}=15I_{sat}$.

A formal treatment of VCC is carried out in Appendix C. An approximate expression for $\bar{n}_j$ (the total population density for a natural mixture of isotopes and spatially averaged over the cell diameter) is

$$\bar{n}_j=\bar{n}_j^{\,0}+\eta(N_j-N_j^0)\pi w_c^2/A_{ef}\ , \tag{9}$$

where N_j is the average population density for a single isotope in the illuminated region (computed in Appendix C).

The factor η accounts for the different isotopic abundances. In Hg, the hyperfine splittings (see Fig. 3) are large compared to the Doppler width. Hence, typically the laser interacts with atoms of a single isotope. The numbers in Fig. 3 correspond to the different isotopes and the letters to the hyperfine structure of the odd isotopes. The even isotopes have zero nuclear moment and thus no hyperfine structure. In naturally occurring mercury, isotope 202 is 30% abundant. Therefore η is equal to 0.3 when the laser is tuned to the transition in isotope 202. The relative abundance of isotope 199 is 17%. Using this and the relative line strength of the hyperfine components of 199 yield $\eta=0.06$ when the laser is tuned to the 199-A transition.

The factor $A_{\rm eff}$ describes an effective area within which the bulk of the $^3P_2$ atoms are confined and is determined by the diameter of the electrodes which were in the form of rings. Experimentally the visible-discharge diameter appears to be slightly larger than the ring-electrode diameter. However, transversely the visible discharge never fills the entire cell. Hence, the assumption of parabolic profiles for the excited-state densities appears to be not applicable. Nonetheless, with that assumption $n_s\equiv n_s(0)=2\bar{n}_s$ and similarly for $n_{q,r}$. Therefore from Eq. (9) and Eqs. (C10)–(C13)

$$n_s=n_s^0-\eta\frac{2\pi w_c^2}{A_{\rm eff}}\frac{1}{1+I'_{\rm op}/I}n_s^0\ , \tag{10}$$

$$n_r=n_r^0+\eta\frac{2\pi w_c^2}{A_{\rm eff}}\frac{\tau_3}{\tau_{23}(\Gamma_{23}+\Gamma_{24})\tau_{\rm eff}}\frac{1}{1+I'_{\rm op}/I}n_s^0\ , \tag{11}$$

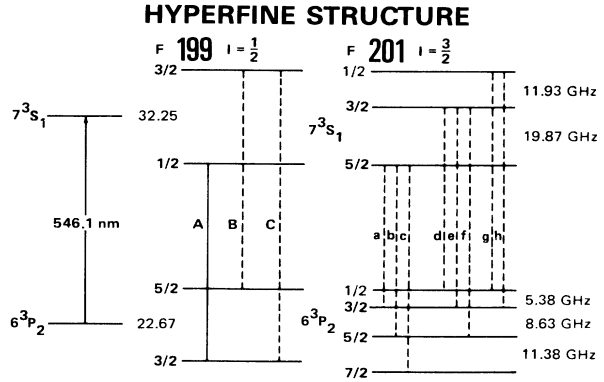

FIG. 3. Hyperfine structure of the odd isotopes for the 6^3P_2 to 7^3S_1 transition. The levels of the even isotopes are not split by the hyperfine interaction. Dashed lines indicate hyperfine transitions that are susceptible to optical pumping. Hyperfine splittings are taken from Rayman (Ref. 15).

$$n_q = n_q^0 + \eta \frac{2\pi w_c^2}{A_{\text{eff}}} \frac{\tau_4}{\tau_{24}(\Gamma_{23}+\Gamma_{24})\tau_{\text{eff}}} \frac{1}{1+I'_{\text{op}}/I} n_s^0 . \quad (12)$$

Using these densities, the electron temperature, rate coefficients (k_{xy}), and E field are recomputed. And the circuit constraint yields the change in current ΔI_D. The change in electron density is obtained from

$$\Delta I_D = I_D - I_D^0 = 0.4 e \mu_e \pi R^2 (n_e E - n_e^0 E^0)$$

which yields

$$\Delta n_e \simeq (\Delta I_D / I_D^0 - \Delta E / E^0) n_e^0 .$$

III. EXPERIMENT

A typical experimental arrangement is shown in Fig. 4. The laser was a Coherent, Inc. 699-21 frequency-stabilized ring dye laser. Measurements of the magnitude of the effect induced by a single beam were made for comparison with the model. The beam was mechanically chopped, typically at frequencies between 250 and 500 Hz, and the signal was detected using a lock-in amplifier. Spectroscopic data was obtained using a single beam and counterpropagating beams. The discharge was obtained by coupling dc or rf power into a cell that contained a few milligrams of naturally isotopic abundant mercury and argon. The argon pressure was varied from 0.01 to 1 Torr while the mercury-vapor pressure (determined by the cell temperature) was estimated to be 6×10^{-3} Torr.

Most of the single-beam measurements were performed in the positive column of a dc discharge. The anode and cathode were made of cylindrical pieces of thin stainless steel ($\frac{1}{16}$ inches thick and approximately $\frac{1}{2}$ inch in diameter). The stainless electrodes were spot welded to tungsten feedthroughs in the glass which provided the electrical connection. Typically, dimensions of the pyrex cell, with quartz windows, were 19 cm long and 2.54 cm in diameter with an anode-to-cathode distance of 10 cm. The length of the positive column L_c varied mainly with argon pressure. Two values for the ballast resistor were used: 10 kΩ or 500 Ω. Often the resistor was placed between the positive terminal of the power supply and the anode, with the blocking capacitor at the anode. In this way, the voltage change across the discharge was monitored directly. Typically, at $p_{\text{Ar}}=0.75$ Torr, $V_{pp}=400$ V, and $I_D=28$ mA, V_D (which includes the cathode fall voltage) was 387 V and L_c was approximately 7.3 cm.

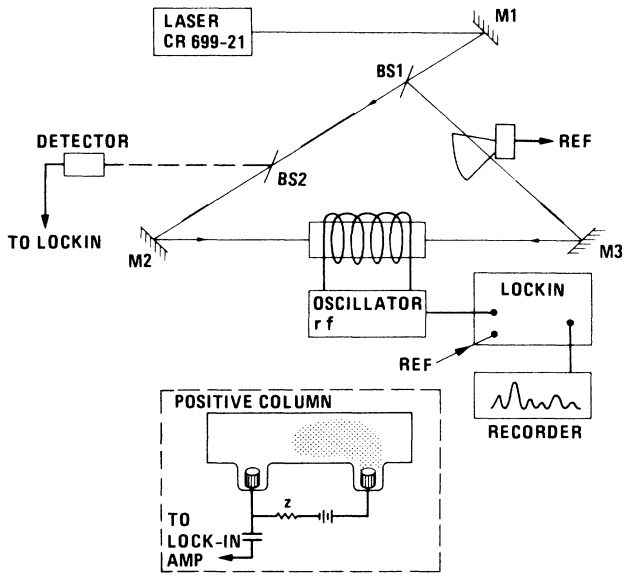

FIG. 4. Typical experimental arrangement. For single-beam measurements one beam is blocked. In Lamb-dip optogalvanic spectroscopy the weak beam is mechanically modulated and the impedance change at the chopping frequency detected.

Measurements were also performed in an rf-induced plasma. This plasma was obtained by coupling power from an oscillator into the cell via a tank circuit. In this case the impedance change was detected by measuring the change in the plate voltage of the oscillator maintaining the discharge—the so-called grid dip technique. The Colpitts-type oscillator was similar to that reported by Lyons.[19] However, our oscillator was capable of delivering more rf power into the cell. This was required in order to produce a Hg-Ar discharge. In our oscillator circuit design,[20] we used a vacuum tube (RCA 6AQ5-A) capable of maintaining higher ac voltages across the cell than those previously reported (3 kV peak to peak as compared to 300 V with the circuit used in Ref. 19).

IV. DISCUSSION OF EXPERIMENTAL DATA AND MODEL ESTIMATES FOR SOME PARAMETERS

In this section theoretical estimates for various parameters are compared with experimental measurements. Parameters that are fairly independent of the plasma response to the disturbance in the level populations are discussed in Sec. IV A, while those that characterize the discharge response to the optical field are discussed in Sec. IV B.

In Sec. IV A measurements of the population of the lower level ($^3P_2$) at very low laser power indicate that the model for the discharge (in the absence of the laser) describes the experimental situation quite well. Additionally, measurements of the saturation intensity indicate that the theory for the laser interaction with the multilevel system, which includes VCC, optical pumping of levels r($^3P_1$) and q ($^3P_0$), and diffusion of atoms into the beam, effectively describes the laser-atomic ensemble interaction.

Measurements of the discharge response to the perturbations in the level populations (Sec. IV B) provide the most stringent test of the theory.

A. Equilibrium populations and saturation intensity

The population difference and saturation intensity are obtained from the intensity-dependent absorption, $\alpha(I)$. Figure 5 depicts the measured absorption versus laser

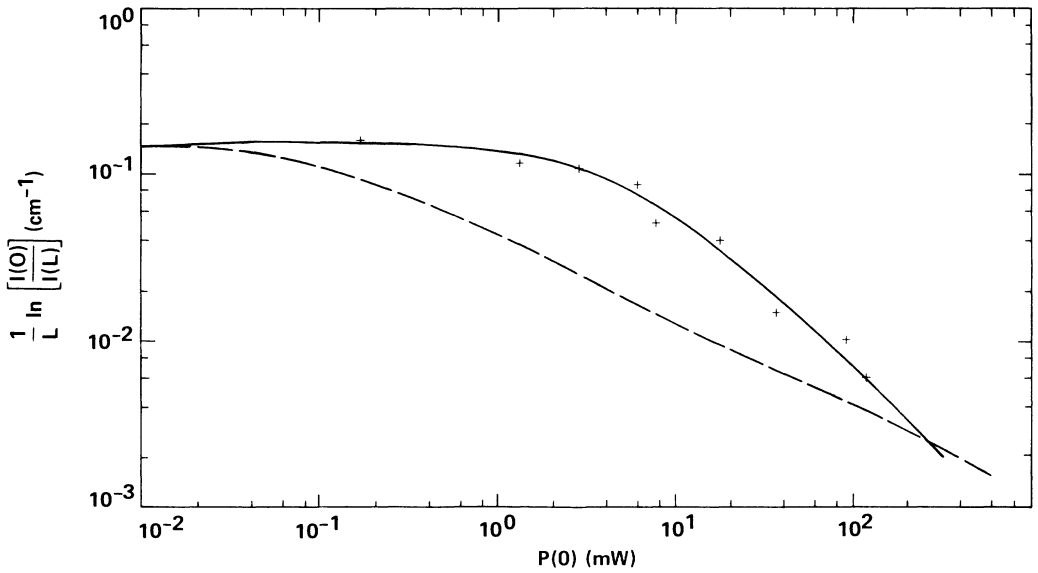

FIG. 5. Absorption as a function of input power with the laser frequency tuned to the A transition in isotope 199. Solid curve is fitted to the experimental data. Dashed curve is the calculated absorption assuming inhomogeneous saturation.

power (P_L) with the laser frequency tuned to the A transition in Hg 199 isotope and discharge parameters $V_D=336$ V, $I_D=28$ mA, $p_{\rm Hg}=0.006$ and $p_{\rm Ar}=0.75$ Torr. The vertical axis in this figure is labeled as $L^{-1}\ln\{I(0)/I(L)\}$ which is equal to $\alpha(I)$ when $\alpha_0 L<1$, where $\alpha_0\equiv\alpha_D^0$ is the Doppler small signal intensity attenuation coefficient.

From the measured α_0, the density difference between the 6^3P_2 and 7^3S_1 is[13] $n_s-n_u=\varepsilon_0\hbar\Delta\omega_D\,\alpha_{T0}/(3\mu^2k)$, where $\alpha_{T0}=\alpha_0/\eta$, $\Delta\omega_D=2\pi\Delta\nu_D$, $\Delta\nu_D=600$ Mhz is the Doppler width and $\mu=(\varepsilon_0hc^3/\tau_u 2\omega^3 g_s)^{1/2}=4.72\times10^{-30}$ C m is the dipole moment. This gives $n_s\simeq1.2\times10^{18}$ m^3 which is within a factor of 2 of model predictions $n_s(0)=2\times10^{18}$ m^3. Other parameters calculated under the same discharge conditions are shown in Table I. In the remainder of Sec. IV A the saturation of the atomic transition is discussed. The reader who is not interested in those details may skip to Sec. IV B.

The best fit to the data was obtained with $\alpha(I)$ equal to $\alpha_{hv}(I)=\alpha_0/(1+I/I_s)$, a homogeneous saturation behavior. This is not usually unexpected for a low-pressure gas with Doppler broadening. The deviation from the expected inhomogeneous saturation behavior is due mainly to VCC. The line-center intensity-dependent absorption, in the absence of VCC, is given by[13]

$$\alpha_D(I)=\alpha_0/(1+I/I_{\rm sat})^{1/2}\ ,$$

where

$$I_{\rm sat}=\frac{c\varepsilon_0\hbar^2}{2\mu^2T_2[\tau_u+(\tau_s-\tau_s\tau_u\gamma_{us})g_u/g_s]}\simeq\frac{\hbar\omega}{(\gamma_{23}+\gamma_{24})\tau_u\sigma(\nu_0)\tau_s}$$

and $\tau_s=n_e^{-1}(k_{sg}+k_{si}+k_{sq}+k_{sr})^{-1}$. Included in $I_{\rm sat}$ is the fact that τ_{us} is not equal to τ_u (i.e., optical pumping of levels 3 and 4 occurs); $I_{\rm sat}$ is the regular saturation intensity (the intensity at which the absorption of the resonant velocity group is half the small signal absorption). To include diffusion of atoms into the beam τ_s is replaced with $\tau_{\rm eff}$, where $1/\tau_{\rm eff}=1/\tau_s+1/\tau_d$ and $\tau_d=w_c^2/(2.4)^2D$ is the diffusion time.

In the presence of VCC and diffusion the line-center absorption, calculated in Appendix C, is approximately equal to

$$\alpha_{Dv}(I,\nu_0)=\alpha_D^0/(1+I/I'_{\rm op})\ ,$$

where $I'_{\rm op}=I_{\rm op}(1+I/I'_{\rm sat})^{1/2}$, $I'_{\rm sat}=\hbar\omega\Gamma_g^v/[(\gamma_{23}+\gamma_{24})\tau_2\sigma_h^0]$, and $I_{\rm op}=\hbar\omega/[(\gamma_{23}+\gamma_{24})\tau_2\sigma_D\tau_{\rm eff}]$.

Typically $I_{\rm op}$ is much less than $I'_{\rm sat}$. Hence it is $I_{\rm op}$ that best describes the saturation behavior of the atomic transition. The other intensity that characterizes the system, $I'_{\rm sat}$, is such that for any $I<I'_{\rm sat}$ the velocity dis-

TABLE I. Calculated values of some parameter under the following discharge conditions: $I_D=28$ mA, $p_{\rm Ar}=0.75$ Torr, $p_{\rm Hg}=0.006$ Torr, and $R=1.27$ cm.

$n_q(0)$	7.1×10^{17} m^{-3}
$n_r(0)$	5.4×10^{16} m^{-3}
$n_s(0)$	2×10^{18} m^{-3}
T_e	12 181 K, 1.05 eV
n_e	2.5×10^{16} m^{-3}
k_{gi}	4.2×10^{-18} m^3/s
k_{qi}	8.9×10^{-16} m^{3}s^{-1}
k_{ri}	1×10^{-15}
k_{si}	1.7×10^{-15}
k_{gq}	3.9×10^{-16}
k_{qr}	9.1×10^{-16}
k_{gs}	1×10^{-15}
E	59.6 V/m
τ_s	84 μs

tribution remains Gaussian. That is, there is no hole burning or Lamb dip when the beams intensities are below I'_{sat}.

To compute I_{op} and I'_{sat} estimates for the effective ground-state lifetime τ_{eff} and VCC rate Γ_{1v} are required. Under the stated discharge conditions, the model yields $\tau_s = 84$ μsec. For such long ground-state lifetimes it is the diffusion time that determines an effective atom-field interaction time. From Ref. 21 $D = 88 p_{Ar}^{-1}$(Torr) cm^2/sec. Using this yields $\tau_d = 21$ μsec and $I_{op} = 5$ mW/cm^2. At higher discharge current, for example, $I_D = 0.4$ A, the model yields $\tau_s = 24$ μsec and diffusion become less important.

An estimate for Γ_{1v} is obtained from the classical expression[13,14] $\Gamma_{1v} = N_{Ar} v_r \sigma_{vcc}$, where N_{Ar} is the density of argon atoms, $v_r = [8kT(m_{Hg} + m_{Ar})/(\pi m_{Hg} m_{Ar})]^{1/2}$ is the relative speed between argon and mercury atoms and σ_{vcc} is the VCC collision cross section. Using the hard-sphere-collision approximation[22] $\sigma'_{VCC} = \pi(r_{Ar} + r_{Hg})^2$, $r_{Ar} = 1.88$ Å, and $r_{Hg} = 1.48$ Å are the radii of argon and mercury atoms, respectively.[23] Typically[24] σ_{vcc} is $7\sigma'_{vcc}$. These estimates yield $\Gamma_{1v} = 33\ 10^6 P_{Ar}$(Torr)sec^{-1} and $I'_{sat} = 1465$ W/cm^2 at $p_{Ar} = 0.75$ Torr.

The above values for I_{op} and I'_{sat} gave a good fit to some data.[20] However, depending on the relative optical and VCC rates, a simple heurestic homogeneous saturation form, as shown by the solid line in Fig. 5, sometimes fits the data. This homogeneous saturation form is graphically close to $\alpha_{Dv}(I)$ in the appropriate limit.

To determine I_s and fit the data, the following procedure was used. At high intensities it is easy to show that regardless of the functional form of $\alpha(I)$, that $L^{-1}\ln[I(0)/I(L)] \simeq \alpha[I(0)]$. Using this I_s is given by $I(0)$ $(L\alpha_0)^{-1}\ln[I(0)/I(L)]$ when $I(0) > \alpha_0 L I_s$. Similarly for $\alpha_D(I)$, I_{sat} is equal to $I(0)\{\ln[I(0)/I(L)]/\alpha_0 L\}^2$, when $I(0) \rangle I_{sat}(\alpha_0 L)^2$. The fitted curve was generated by computing $I(L)$ using the approximate saturation intensity and α_0 in the *solution* to $dI/dz = -\alpha(I)I$. A root-finding procedure was necessary to determine $I(L)$, since the solution to the Beer's-law equation is a transcendental equation.

A measured saturation power P_s, which is equal to 4.3 mW, was obtained from the fit. This yields an average saturation intensity $I_s = P_s/(\pi w_c^2) = 96$ mW/cm^2, where $w_c = 1.2$ mm is the Gaussian beam radius at the cell. On the 202 component P_s was measured to be 5.5 mW. The dashed line in Fig. 5 is the inhomogeneous saturation $[\alpha_D(I)]$ that was expected. The dashed curve is plotted using a saturation power of $P_{sat} = 66$ μW ($I_{sat} = 1.5$ mW/cm^2), a value that was obtained from measurements in a pure Hg discharge.

To decouple the predicted plasma response (due to the population redistribution) from the approximations necessary to obtain I_{op} and I'_{sat}, the measured saturation intensity instead of I'_{op} was used in Eqs. (10)–(12).

B. Magnitude of the signal induced by a single beam

The measured and predicted change in discharge voltage when the laser was tuned to the 199A and then 202 components are shown in Fig. 6. The agreement is good particularly below the highest powers. A corresponding plot of ΔV_D versus the measured absorbed laser power (P_{abs}) was best fitted with a straight line. Hence, the discharge is responding linearly to the optical field. Additionally, the optogalvanic effect parameter O_e [defined as the change in power delivered to the ballast resistance divided by the absorbed power (Doughty *et al.*[6])] versus absorbed power is roughly constant and has a value of -0.5.

Figure 6 also shows that at very high laser power, ΔV_D continues to increase even though the population difference between the $^3P_2$ and $^3S_1$ states saturates. This is because additional depletion of the lower state ($^3P_2$) can still occur at very high laser power, even though the population difference saturates at medium power. The mechanism that allows addition depletion of the lower level is most likely due to a combination of VCC and power broadening. At high optical power, more atoms interact with the laser because the power-broadened linewidth is effective in capturing more atoms through VCC. The lifetime of the upper states fixes the resonant velocity group population of the lower level and hence the population difference.

It can also be inferred from the preceding arguments that in some cases the OGE is a more sensitive probe of level populations than absorption measurements. This is especially true in cases where the OGE strongly depends on the population of a single level, as opposed to the absorption which monitors the population difference.

Some inaccuracy of the theoretical predictions of the OGE is expected at very high laser power, since an approximate form for N_j was used instead of the more exact expression derived in Appendix C. Also the contribution of the steady-state population in the upper state (7^3S_1) to the ionization process was ignored in the model. In addition, the rich variety of associative ionization

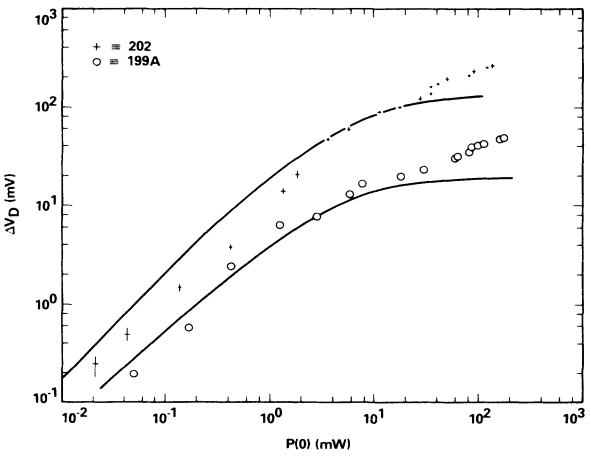

FIG. 6. Change in the discharge voltage vs laser power when the laser frequency is tuned to the transitions in isotopes 202 and 199. Discharge parameters are $I_D = 28$ mA, $P_{Ar} = 0.75$ Torr, $P_{Hg} = 0.006$ Torr, $R = 1.3$ cm. Solid curves are model predictions.

processes,[12] probably important when the $^3P_2$ population is significantly depleted (that is, at high laser power), were not considered.

As shown previously, VCC assist in the laser-induced redistribution of the population; hence VCC affect the magnitude of the OGE. In our case VCC lead to an increase in the OGE signal. Comparison of measurements at a high optical power in a pure Hg and Hg-Ar discharge show that the impedance change increased by a factor of 10.

The predicted changes in electron temperature and density when the laser was tuned to the 199A transition are shown in Fig. 7. A change in T_e has been observed previously in various discharges but not entirely explained. An increase in the electron temperature was reported by Kenty.[9] Furthermore, Dreze *et al.*[25] measured ΔT_e when a uranium discharge was illuminated. Arimondo[26] utilized the change in electron temperature for optoacoustic spectroscopy. Despite these observations, the mechanism responsible for such a change is still not understood. In Ref. 25 it was suggested that T_e increases because part of the laser power is funneled into the electron gas as a result of superelastic collisions between atoms in the laser excited level and electrons. However, an accounting of the energies involved would show that such a mechanism is unlikely. Furthermore, that mechanism cannot explain an increase in T_e when the overall effect of the optical field is to pump most of the atoms into a state that is lower in energy (in our case $^3P_1$, $^3P_0$, and 6^1S_0) than the initial state ($^3P_2$). In our experiment an increase in fluorescence from an argon line at 810.4 nm was observed when the laser frequency was on an atomic resonance (546.1 nm). This increased laser-induced fluorescence (LIF) could probably be ascribed to an increase in T_e.

We believe that the change in electron temperature occurs because the ionization and loss rates depend differently on the optical field. The rate of electron and ion loss is fairly independent of the optical field and depends mainly on the diffusion coefficients and cell diameter. In low pressure (<10 Torr) and low current density (<1 A/cm^2) discharges such as the type discussed here, electron recombination within the plasma is negligible and electron loss occurs mainly at the walls. The ionization rate, however, depends on the optical field. The laser removes ^3P atoms and hence lowers the ionization rate. To restore equality between the generation and loss rates and avoid an ion-deficient plasma, the electric field increases and on average dumps more electrical power into the electron gas, increasing the electron temperature.

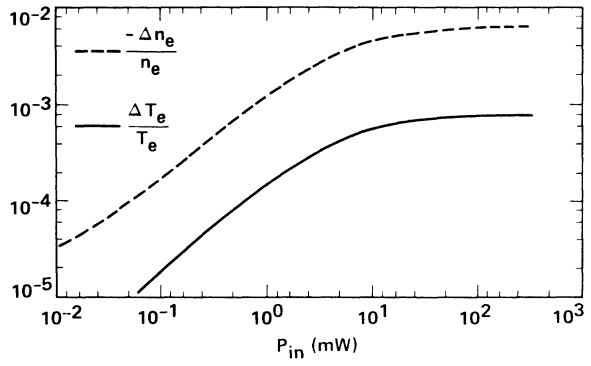

FIG. 7. Predicted change in electron temperature and electron density as a function of input optical power with the laser frequency tuned to the 199-Å transition. Discharge parameters are identical to those in Fig. 6.

It is important to be able to predict the change in electron temperature, since for the design of any device that may be based on the OGE (such as an opening switch) one should know how much the ionization rates can be changed and what limits the change in electron temperature. If ΔT_e is ignored and the OGE assumed to be due only to population redistribution, the estimated change in current is roughly 30% below the value obtained when ΔT_e is included. The model further estimates that the change in electron temperature is almost independent of discharge current. However, the change in electron density depends on I_D.[27]

Figure 8 shows the predicted change in voltage and T_e as a function of argon pressure at fixed input optical power. Note that the change in T_e is nearly independent of argon pressure as expected from the explanation for the change in T_e. The long settling time for the discharge after a change in argon pressure prevented the taking of reliable data to confirm these predictions.

The calculated changes in current as a function of I_D at two different input optical powers are shown in Fig. 9. Calculated values are generally within a factor of 10 of measurements. An order of magnitude agreement is fairly good given the gross assumptions made and the absence of any free parameter. An assumption that is questionable and correctable is the Maxwellian function for the electron-energy distribution. Throughout the current range employed ($0<I_D<100$ mA) the electron-

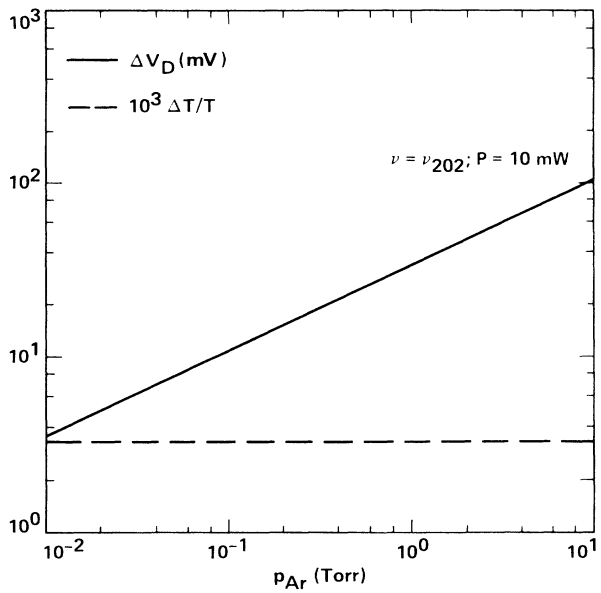

FIG. 8. Predicted change in I_D and T_e vs argon pressure when $P_{in}=10$ mW.

energy-distribution function is hardly Maxwellian. However, that assumption is gross at extremely low currents, $I_D < 15$ mA. Hence, when I_D is less than 15 mA, agreement between theoretical predictions and measurements for population densities and ΔI_D, etc., is not expected. A possible correction for this is to employ a two- or three-electron group distribution function.[28]

Referring to Fig. 9(a), the disagreement observed when $P(0)$ is equal to 11 mW can be qualitatively understood. The OGE is expected to be smaller than the predicted value at low laser beam transmission and/or at high discharge currents ($\alpha_0 L \gg 1$). This is because of the longitudinal inhomogeneity of the absorption. The discharge response to local perturbations may be different from that for uniform perturbations. A local perturbation of the population, such as that which occurs at the entrance face of the cell when the absorption is high, would probably cause a response from the local inhomogeneities in the electric field.

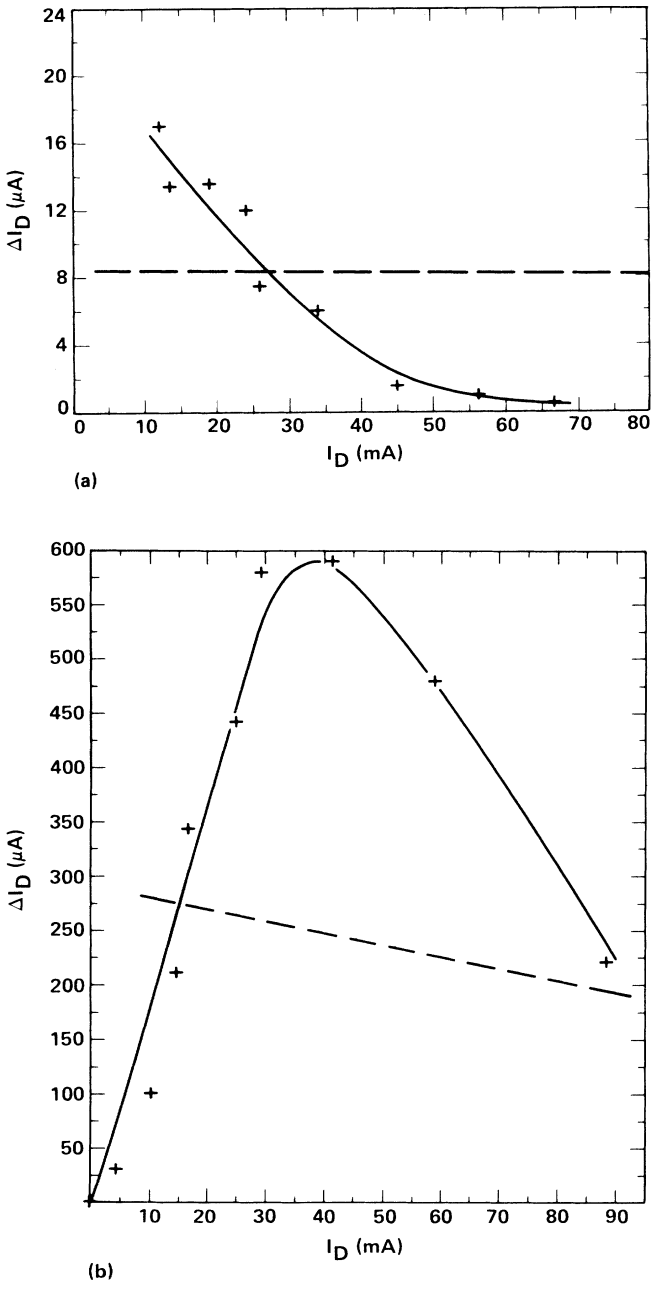

FIG. 9. Measured and estimated *change* in discharge current vs total discharge current I_D with the laser frequency tuned to the 202 transition. Dashed lines are the theoretical estimates and the solid line is a fit to the data. (a) $P_{in} = 11$ mW and $Z = 10\ k\Omega$, (b) $P_{in} = 256$ mW and $Z = 500\ k\Omega$.

At high input power, $P(0) = 184$ mW, other effects as previously described become important and any agreement seen in Fig. 9(b) may be fortuitous.

V. OPTOGALVANIC SPECTRA

In this section, experimental single-beam Doppler-limited and Doppler-free optogalvanic spectra are presented. In some of the Doppler-free spectra, the influence of VCC is evident. Also presented are some peculiarities of the impedance change observed with counterpropagating beams.

A. Single-beam spectra

Figure 10 illustrates the optogalvanic signal obtained in an rf discharge, with a single beam. In Fig. 10(a) the rf field from the Colpitts oscillator was kept at the minimum required to maintain the discharge ($\alpha_0 L < 0.6$) and the optical power was also at a minimum. The labeling corresponds to the transitions shown in Fig. 3. In Fig. 10(b) the metastable ($^3P_2$) density was increased. The relative amplitudes of the signal on the different components is different than in Fig. 10(a) because of the longitudinal inhomogenity of the absorption. At higher power, $P(0) < 400$ mW, the signal does not display reversals of the type observed by Kane.[29] A typical spectrum with $P = 48$ mW is shown in Fig. 10(c).

B. Doppler-free spectra

Using counterpropagating beams, it is possible to obtain Doppler-free spectra and probe many aspects of the laser-atomic ensemble interaction. Figures 11 and 12 show the optogalvanic signal due to a chopped weak probe in the presence of a strong continuous counterpropagating pump beam. Only the impedance change at the chopping frequency is detected by the lock-in amplifier.

In spectra obtained in the positive column of a dc discharge ($P_{Ar} = 0.75$ Torr), Fig. 11, the relative amplitudes of the single-beam signal are close to that calculated by considering line strength and isotopic abundances[15] and agree with those in Fig. 10(a). The drastic reduction of the signal over the entire Doppler distribution as the pump-beam intensity is increased dramatically illustrates the presence of VCC.

Collisions between $^3P_2$ atoms and argon atoms are assumed to be (i) phase interrupting in their effect on the Hg atom wave function and (ii) velocity changing in their effect on level populations. The phase-interrupting effect of the collision leads to pressure broadening

($\simeq$10.4 MHz/Torr).[30] On the other hand, the velocity-changing effect of a collision tends to thermalize the velocity distribution of the level population. It is possible to have collisions that are phase interrupting and not velocity changing. Figure 13 illustrates how the probe interaction with the atomic system is affected when a strong counterpropagating beam is present and the

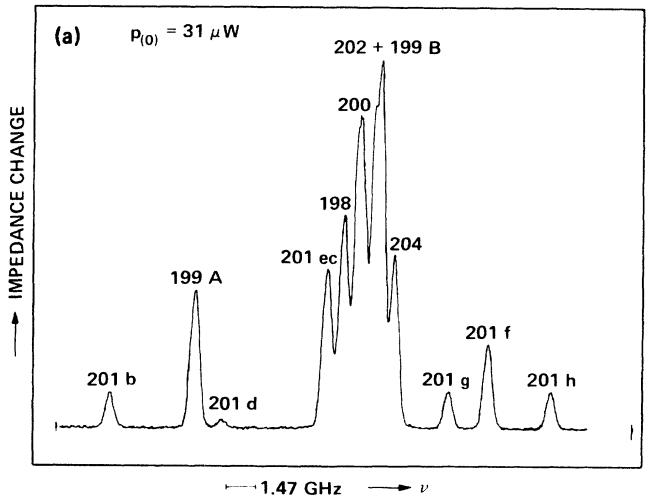

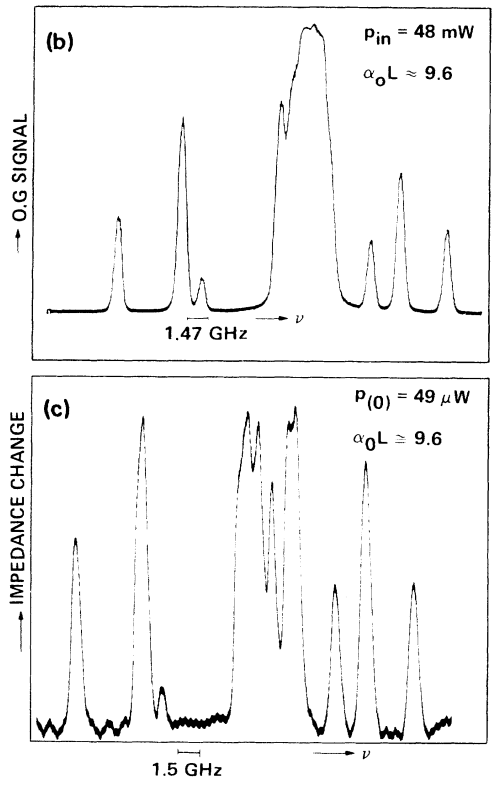

FIG. 10. (a) Single-beam optogalvanic spectra at low input optical power and a weak discharge. (b) and (c) Single-beam optogalvanic spectra at different discharge and optical power levels.

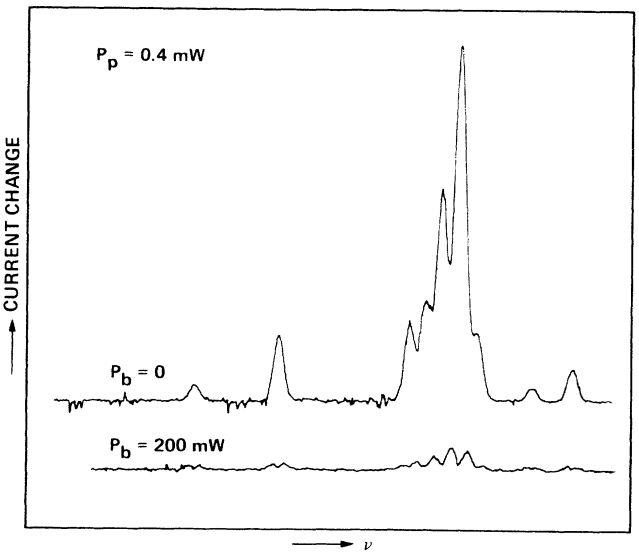

FIG. 11. Current change due to a chopped weak beam in the presence of a strong continuous counterpropagating pump beam. Medium is the positive column of a dc discharge.

atoms are subjected to VCC. It is now clear that the drastic reduction of the signal seen in Fig. 11 confirms the presence of VCC.

In Fig. 12 the spectrum was obtained with an rf discharge at an argon pressure lower than in the dc discharge and $\alpha_0 L$ was 10.4. The overall reduction of the signal on the introduction of a counterpropagating beam was previously explained. Other distinctive features in Fig. 12 are the impedance Lamb dips on the

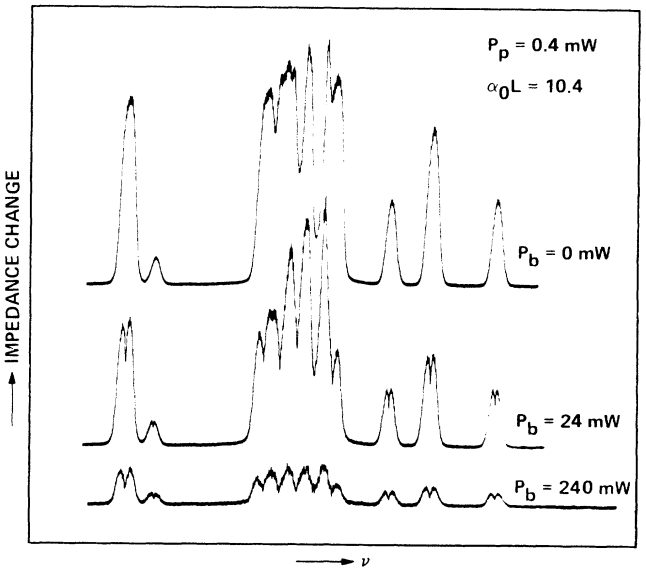

FIG. 12. Impedance change in an rf discharge with the optical arrangement as in Fig. 11.

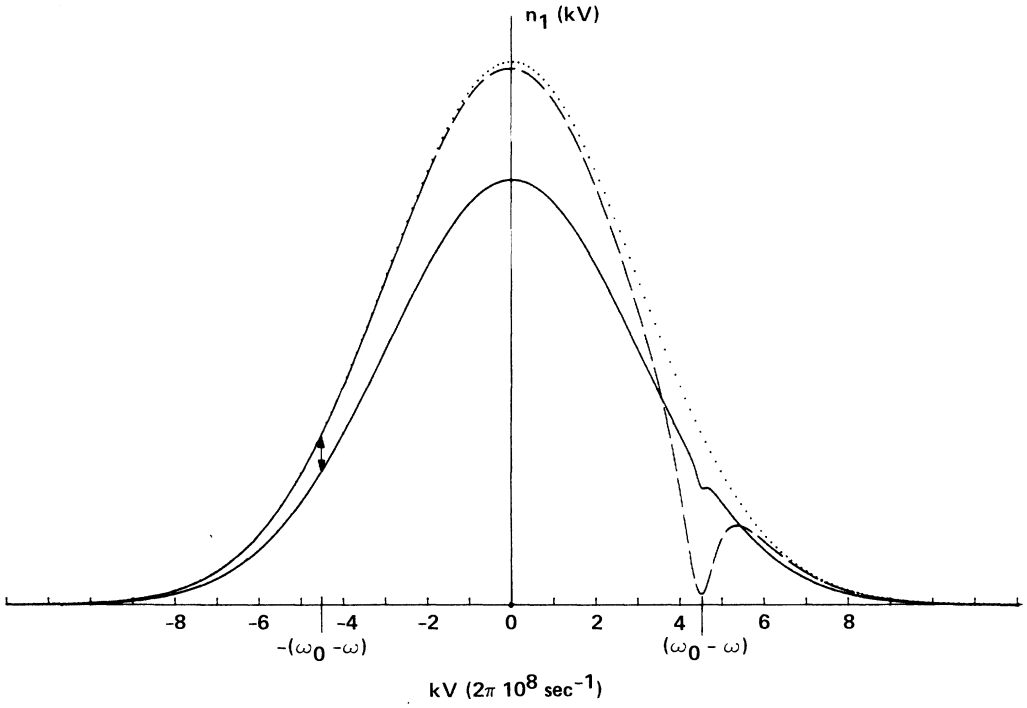

FIG. 13. Velocity distribution of atomic level population when the ensemble is interacting with counterpropagating beams of the same frequency. The dotted curve is the velocity distribution when the input optical power is zero. The dashed curve is the distribution with laser frequency tuned off line center, the optical power above the saturation intensity, and no VCC. The solid curve is the distribution when the effects of VCC are included.

introduction of the backward propagating pump beam. Optogalvanic Lamb dips are also present in Fig. 11.

Doppler-free optogalvanic Lamb dips occur as in saturation spectroscopy, when both beams interact with atoms of the same velocity group. That is, when the laser frequency is tuned off resonance (see Fig. 13) the forward propagating ($+z$ direction) probe beam interacts only with atoms whose longitudinal (parallel to the laser beam) component of velocity is within $2\pi\Delta\nu/k$ of $v_+=(\omega-\omega_0)/k$. The backward beam interacts with atoms of opposite longitudinal velocity $v_-=-(\omega-\omega_0)/k$. As the laser frequency is tuned on to resonance ($\omega=\omega_0$) both beams interact with the same group of atoms. The pump beam saturates the transition. Hence the number of atoms removed by the probe beam is less than when the pump beam was absent. As far as sensitivity goes, the signal-to-noise ratio of Lamb-dip optogalvanic spectroscopy is less than that obtained using saturation spectroscopy.

C. Anomalous features observed using counterpropagating beams

Some features of the optogalvanic signal not yet understood have been observed when the counterpropagating beams arrangement is employed. In an rf discharge the impedance change (again due to a chopped weak probe in the presence of a strong continuous counterpropagating beam) is shown in Fig. 14. The reduction of the signal at high power and the Lamb dips were previously explained. However, on the 202 component in Fig. 14(b) the impedance change appears to reverse on line center. Under different discharge conditions a definite reversal of the signal was observed on all components. These reversals were observed only in an rf discharge and the exact discharge conditions that permit such a reversal are not yet clear. Under the appropriate conditions such spectra may be observed repeatedly. However, achieving the proper discharge conditions was difficult and obtained only $\sim 5\%$ of the time.

When these reversals occurred, the monitored laser-induced fluorescence at 546.1 and 435.8 nm and the transmitted probe showed normal Lamp dips. This means that the reversals are not due to optical effects but to the discharge response to changes in the atomic level population. It is likely that the source of the reversal is the competition between two different ionization processes that contribute to the signal.

Possible competitive mechanisms are (1) population redistribution, (2) the change in T_e, (3) associative ionization, and (4) two-step ionization through the upper level. The actual mechanism is probably an interplay between these effects. As previously pointed out, the reduction of the metastable density leads to a decrease in the density of electrons generated. However, the corresponding increase in T_e tend to increase the density of electrons generated, albeit from other levels. On illumination of the discharge, the $^3P_0$ and $^3P_1$ populations increase. Associative ionization such as $6^3P_0+6^3P_1\rightarrow Hg_2^++e$ and $6^3P_2+6^3P_1\rightarrow Hg^*+e$ fol-

lowed by $Hg^* + e \rightarrow Hg^+ + 2e$ tend to increase the density of electrons generated. Additional data are needed to assess the relative contribution of the various processes under the stated conditions. Kane[29] has observed sign reversal in the optogalvanic signal using a single beam. Van de Weijer *et al.*[27] using nanosecond pulses have also observed sign reversals in the optogalvanic signal.

Another very interesting feature in the impedance change is the almost chaotic behavior which may occur for some discharges on the introduction of a strong counterpropagating beam as shown in Fig. 15. These effects occur even more often than the reversals—as often as 10% of the time.

VI. SUMMARY

In this paper, a theoretical description of the optogalvanic effect induced in the positive column of a Hg-Ar discharge by light at 546.1 nm was presented. In a detailed description of the laser interaction with the multilevel atomic system it was necessary to take into account velocity-changing collisions. The effects of those collisions were observed in optogalvanic spectra, saturation spectroscopy and in measurements of the intensity-dependent absorption. Measurements of the magnitude of the optogalvanic signal (induced by a single beam) as a function of laser power and discharge current show fairly good agreement with theory.

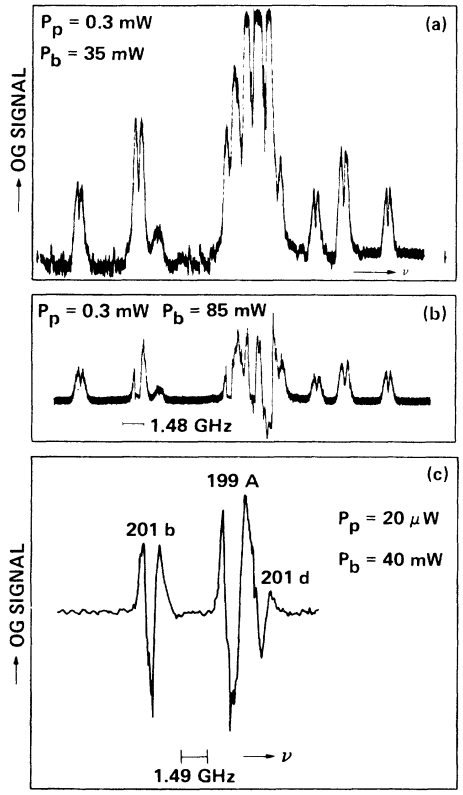

FIG. 14. Impedance change due to a weak probe beam in the presence of a strong counterpropagating pump beam. Spectra under conditions showing reversal of the impedance change on line center.

Also advanced was an explanation for the change in the electron temperature that occurs when the discharge is illuminated. The change in the electron temperature occurs because the electron-loss rate is fairly independent of the optical field while the ionization rate depends on the optical field.

Finally, in the optogalvanic signal obtained using two beams, some novel features were observed. It was observed that the impedance change due to a weak beam on resonance can be reversed by the introduction of a strong counterpropagating beam. Additionally the impedance change due to a weak beam can become chaotic on the introduction of a strong counterpropagating beam. The authors would like to thank Mr. Juergen Linke for skillfully preparing the glassware. The research described in this paper was performed at the Jet Propulsion Laboratory, California Institute of Technology, under contract with the U. S. National Aeronautics and Space Administration. One of us (E.G.) was partially supported by the National Science Foundation.

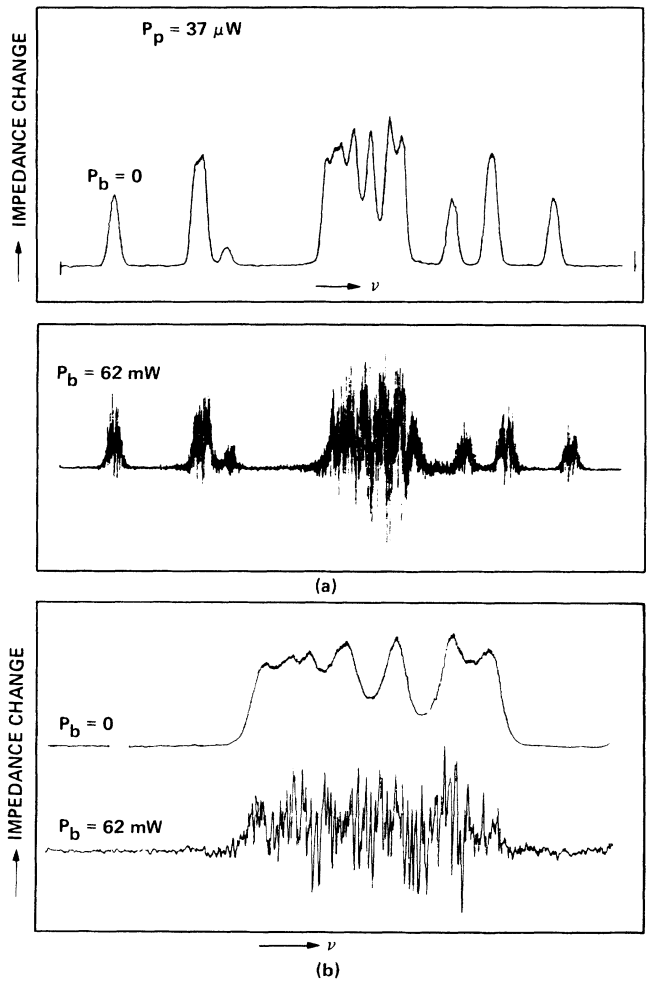

FIG. 15. Anomalous spectra of the impedance change due to a weak beam on the introduction of a strong backward beam in an rf discharge.

TABLE II. Notation used in this paper.

n_x $(x=g,q,r,s,i)$	Total population density of level x
n_y $(y=1,2,3,4)$	Velocity-dependent population density of a single isotope and/or hyperfine level
D_a	Ambipolar diffusion coefficient
$\nu_{\rm col}$	Electron-argon collision frequency
μ_e	Electron mobility
χ	Fractional energy loss per electron per elastic collision with an argon atom
k_{xy}	Rate coefficient for electron-collision-induced transition from level x to y
E	Electric field in the positive column
$P_{\rm Ar}$	Argon pressure
m	Electron mass
$m_{\rm Ar}$	Mass of an argon atom
σ_{xy}	Collision cross section for the atom transition from level x to y; for upward transitions $\sigma_{xy}=\sigma^0_{xy}(\varepsilon_y-\varepsilon_x)$
I_ν	Intensity of the laser at frequency ν
W_c	Gaussian beam radius at the discharge cell
γ_{2j} $(j=1,3,4)$	Transition probability from level 2 to j
$\sigma(\nu)$	Optical absorption cross section
$I_{\rm sat}$	The saturation intensity in the absence of cross relaxation
$I'_{\rm sat}$	A characteristic intensity of the medium when velocity-changing collisions are important; at intensities below $I'_{\rm sat}$ the velocity distribution remains Gaussian
$I_{\rm op}$	Another characteristic intensity of the medium when velocity-changing collisions are important
I_s	The saturation intensity obtained when the homogeneous saturation form is used to fit the data
D	Diffusion constant of mercury atoms in argon

APPENDIX A

See Tables II and III for the notation and the numerical values of some of the parameters used in this paper.

APPENDIX B

See Fig. 16 for a flowchart of the calculations.

APPENDIX C

In this appendix, the effects of VCC on the laser interaction with the atomic level populations are considered. Derived are the populations in the presence of the optical field and intensity-dependent absorption.

The rate equations that describe the laser interaction with the atomic level populations (see Fig. 1) are

$$\frac{\partial n_1}{\partial t}=R_1-\frac{\sigma(\nu)I_\nu}{h\nu}\left[n_1-\frac{g_1}{g_2}n_2\right]+\frac{n_2}{\tau_{21}}-\gamma_1 n_1+D\nabla^2 n_1 + \left[-\Gamma_{1v}n_1+\int dv' W_1(v'\rightarrow v)n_1\right], \quad \text{(C1)}$$

$$\frac{\partial n_2}{\partial t}=\frac{\sigma(\nu)I_\nu}{h\nu}\left[n_1-\frac{g_1}{g_2}n_2\right]-\frac{n_2}{\tau_2}, \quad \text{(C2)}$$

$$\frac{\partial n_3}{\partial t}=R_3-\gamma_3 n_3+\frac{n_2}{\tau_{23}}-\frac{n_3}{\tau_r}, \quad \text{(C3)}$$

TABLE III. Numerical values of some parameters. The asterisk denotes the values for the discharge parameter that were obtained from Ref. 11, which also lists the original source.

Discharge parameters

Parameter	Process
$\sigma_0=d\sigma/d\varepsilon$ $(10^{-20}$ m^2/eV)	
4	$^3P_j+e\rightarrow Hg^++2e$, $j=q,r,s$
1	$6^1S_0+e\rightarrow Hg^++e$
0.7	$6^1S_0+e\rightarrow 6^3P_0+e$
k_{sr}	10^{-13} m^{-3} sec^{-1}
$k_{sq}=k_{sr}$	
$k_{rq}=0.75k_{sr}$	
ν_0^*	1.5×10^9 sec^{-1} V$^{-1.65}$ Torr^{-1}
μ_e^*	306 m^2 V$^{-0.5}$ sec^{-1}
μ_i	0.134 m^2 V$^{-0.5}$ sec^{-1}

Optical Parameters

Parameter	Value
τ_2	8.8 nsec
$\tau_{21}=1/\gamma_{21}$	18 nsec
$\tau_{23}=1/\gamma_{23}$	25 nsec
$\tau_{24}=1/\gamma_{24}$	56 nsec
σ_h^0	9.6 10^{-15}m^2
σ_D	6.5 10^{-16}m^2
D	165 cm^2/sec (at 0.75 Torr Ar)
u (mean velocity)	194 m/sec ($\Delta\nu_D=600$ mHz)

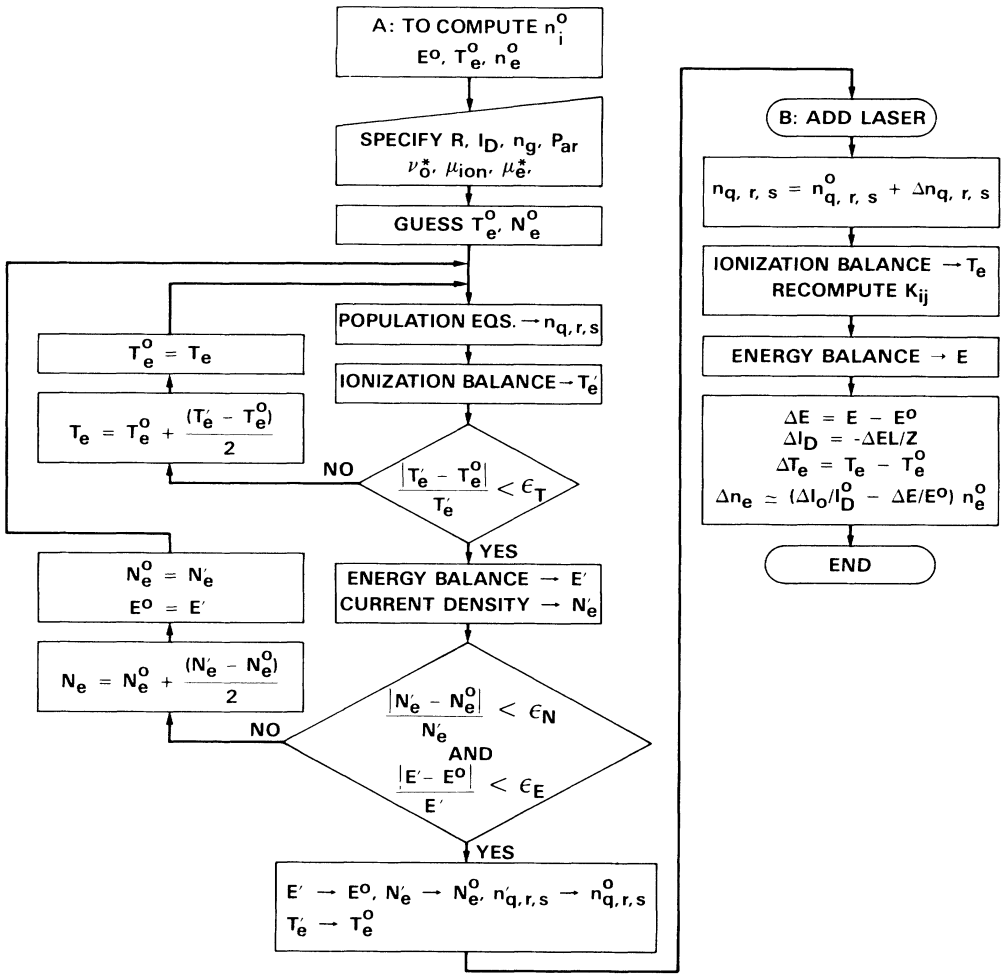

FIG. 16. Flowchart of calculations.

$$\frac{\partial n_4}{\partial t} = R_4 - \gamma_4 n_4 + \frac{n_2}{\tau_{24}} \ . \tag{C4}$$

The approach to treating VCC here is similar to that employed in Refs. 17 and 31. The essential difference between the treatment here and other approaches is that the effect of VCC on the upper level is ignored in the rate equations. This permits a direct solution of the rate equations in a noniterative manner.

The velocity-dependent populations are indicated by n_j $(j=1,2,3,4)$. Also n_j refers to that population of the specific isotope hyperfine levels that are coupled by the laser. For example, when the laser is tuned to the A transition in isotope 199, then level 1 refers to the $F=3/2$, 6^3P_2 level and level 2 to the $F=1/2$, 7^3S_1 level. Typically the hyperfine splittings are much larger than the Doppler width. Therefore the laser interacts only with atoms of a particular isotope. The total population of level j is $N_j = \int n_j\, dv$. In the absence of the optical field, the equilibrium populations are $n_j^0 = N_j^0 G(x)$, where

$$G(x) = e^{-(x/ku)^2}/(\pi^{1/2} ku) \quad \text{and} \quad x = kv \ .$$

Because of the short lifetime of the excited state, an excited atom decays before it experiences a collision. Hence cross relaxation in the excited state can be ignored. The effects of VCC's on the levels not directly connected to the laser, levels 3 and 4, have also been ignored.

In the strong-collision approximation $W_1(v' \to v) \simeq W_1(v)$ and $W_1(v) = \Gamma_{1v} G(x)$ where Γ_{1v} is the rate at which VCC's occur.

The term $D\nabla^2 n_1$ describes diffusion of unpumped atoms into the beam. A reasonable assumption is that $n_1(r) = n_1^0$ for $r \geq a$ and $n_1(r) = n_1^0[1 - J_0(2.4r/a)]$, $r \leq a$ where $a \simeq W_c$ (W_c is the beam radius at the cell) and D is the diffusion constant of $^3P_2$ atoms in argon. The diffusion term can be approximated by $-(n_1 - n_1^0)/T_d$, where with the above assumption, the diffusion time $T_d = (a/2.4)^2/D$. The cell radius R is much larger than the beam radius W_c. Spatially averaging over the illuminated region removes the spatial dependence. However, the minor constants from spatial averaging are ignored.

Additionally the incoherent pumping rates R_j are taken to be constant. That is, the change in the electron temperature induced by the laser is ignored. In relation

to the equations in the main body of Sec. II $R_1 \simeq n_e(k_{gs}n_g + k_{qs}n_q + k_{rs}n_r)$ and $\gamma_1 \simeq n_e(k_{sg} + k_{sq} + k_{sr} + k_{si})$ and similarly for the other R_j.

Therefore in the steady state Eqs. (1) and (2) become

$$0 = R_1 - \Gamma_L \left[n_1 - \frac{g_1}{g_2} n_2 \right] + \frac{n_2}{\tau_{21}} - \gamma_1 n_1 - \frac{(n_1 - n_1^0)}{T_d} + (W_1 N_1 - \Gamma_{1v} n_1) , \tag{C5}$$

$$0 = \Gamma_L \left[n_1 - \frac{g_1}{g_2} n_2 \right] - \frac{n_2}{\tau_2} , \tag{C6}$$

where

$$\Gamma_L = \frac{\sigma(\nu) I_\nu}{h\nu} = \frac{\sigma^0 I}{h\nu} \frac{\gamma_h^2}{(\Delta - x)^2 + \gamma_h^2}$$

and $\sigma^0 = \lambda^2 g_2 2/(\tau_{21} 8\pi g_1 \pi \Delta\nu)$, $\Delta = \omega - \omega_0$, ω is the laser frequency, ω_0 the atomic transition frequency, and $\gamma_h = \pi\Delta\nu = [1/(2\tau_2) + \gamma_p]$. The homogeneous linewidth $\Delta\nu$ includes the contribution due to pressure broadening γ_p. Also $1/\tau_2 = 1/\tau_{21} + \Gamma_{2m}$ where $\Gamma_{2m} = 1/\tau_{23} + 1/\tau_{24}$ and $g_{12} = g_1/g_2$. From (5) and (6) we obtain

$$n_1 = \frac{(g_{12}\Gamma_L + 1/\tau_2)[N_1^0(\gamma_1 + 1/T_d) + \Gamma_{1v} N_1] G(x)}{\Gamma_L(g_{12}\gamma_1' + \Gamma_{2m}) + \gamma_1'/\tau_2} , \tag{C7}$$

where $\gamma_1' = \gamma_1 + 1/T_d + \Gamma_{1v}$.

In the Doppler limit, power-broadened linewidth much less than the Doppler width, Eq. (7) is integrated over the velocity distribution. The integration yields

$$N_1 = [N_1^0(\gamma_1 + 1/T_d) + \Gamma_{1v} N_1] \times \left[\frac{G(\Delta)\pi}{\gamma_{pb}} \left[\frac{g_{12}\tau_2 \sigma^0 \gamma_h^2 I}{\gamma_1' \hbar\omega} + \frac{\gamma_h^2}{\gamma_1'} \right] + \frac{G(\Delta)}{\gamma_1'} (\pi^{1/2} ku - \pi\gamma_{pb}) \right] , \tag{C8}$$

where

$$\gamma_{pb}^2 = \gamma_h^2 (1 + I/I'_{\text{sat}})$$

and

$$I'_{\text{sat}} = \frac{\hbar\omega\gamma_1'}{\sigma^0 \tau_2 (g_{12}\gamma_g + \Gamma_{2m})} .$$

The important rates and times that determine how effective VCC are in thermalizing the population are the effective ground-state lifetime τ_{eff}, the rate of VCC Γ_{1v}, and the rate at which atoms are leaving the resonant system Γ_{2m}. Now with $\tau_{\text{eff}} = 1/(\gamma_1 + 1/T_d)$, it follows that $\Gamma_{1v}/\gamma_1' \simeq 1 - 1/(\tau_{\text{eff}}\Gamma_{1v})$, because typically $\tau_{\text{eff}}\Gamma_{1v}$ is much larger than one. Using this, Eq. (8) yields

$$N_1 = N_1^0 \frac{I'_{\text{op}}}{I'_{\text{op}} + I} \left[1 - \frac{I}{I'_{\text{op}} \gamma_1' \tau_{\text{eff}}} \right] , \tag{C9}$$

where

$$I_{\text{op}} = \frac{\hbar\omega}{\sigma_D \tau_2 \tau_{\text{eff}} (\gamma_{23} + \gamma_{24})} , \quad \sigma_D = \sigma^0 \gamma_h \pi G(\Delta)$$

and

$$I'_{\text{op}} = I_{\text{op}} (1 + I/I'_{\text{sat}})^{1/2} .$$

The integral in Eq. (7) was evaluated in the limit $\gamma_{pb}/ku \ll 1$. It can be shown that within that limit $I/(I'_{\text{op}}\gamma_1'\tau_{\text{eff}})$ is less than 1. Therefore

$$N_1 = \frac{I'_{\text{op}}}{I'_{\text{op}} + I} N_1^0 . \tag{C10}$$

Similarly,

$$N_2 = \frac{I}{(I'_{\text{op}} + I)} \left[\frac{N_1^0}{\tau_{\text{eff}}(\gamma_{23} + \gamma_{24})} \right] , \tag{C11}$$

$$N_3 = N_3^0 + \frac{\tau_3}{\tau_2} \left[\frac{I}{I'_{\text{op}} + I} \right] \frac{N_1^0}{\tau_{\text{eff}}(\gamma_{23} + \gamma_{24})} , \tag{C12}$$

$$N_4 = N_4^0 + \frac{\tau_4}{\tau_{24}} \left[\frac{I}{I'_{\text{op}} + I} \right] \frac{N_1^0}{\tau_{\text{eff}}(\gamma_{23} + \gamma_{24})} . \tag{C13}$$

The velocity-dependent population $n_1(kv)$ is obtained by substituting (10) into (7), and $n_2(kv)$ is obtained from Eq. (6) and $n_1(kv)$. Defining $\mathcal{L}_{pb}(x) = \gamma_{pb}^2/[(\Delta - x)^2 + \gamma_{pb}^2]$, this yields

$$n_1(x) = G(x) N_1^0 \left[\frac{I'_{\text{op}}}{I + I'_{\text{op}}} \right] \times \left[1 - \frac{I}{I + I'_{\text{sat}}} \mathcal{L}_{pb}(x) \times \left[1 - \frac{g_{12}\gamma_1'}{(g_{12}\gamma_1' + \Gamma_{2m})} \right] \right] ,$$

$$n_2(x) = G(x) N_1^0 \left[\frac{I'_{\text{op}}}{I + I'_{\text{op}}} \right] \left[\frac{I}{I + I'_{\text{sat}}} \right] \times \frac{\Gamma_{1v}}{(g_{12}\gamma_1' + \Gamma_{2m})} \mathcal{L}_{pb}(x) .$$

The intensity-dependent absorption is given by

$$\alpha(I,\nu)=\int dv\,\sigma_h(n_1g_2/g_1-n_2)$$
$$\simeq\sigma_D N_1^0/(1+I/I'_{\rm op})$$
$$\times\left[1-\zeta\frac{I/I'_{\rm sat}}{(1+I/I'_{\rm sat})^{1/2}}\times\frac{1}{1+(1+I/I'_{\rm sat})}\right], \quad \text{(C14)}$$

where

$$\zeta\simeq\frac{(\Gamma_{2m}-\Gamma_{1v})}{(\Gamma_{2m}+\Gamma_{1v})}.$$

Depending on the relative optical pumping rate (Γ_{2m}) and VCC rate, some simplification of the intensity-dependent absorption formula is possible. For example, when Γ_{2m} is comparable to Γ_{1v} (as is the case in Hg for argon gas pressure above 0.5 Torr) then the last term in (C14) can be ignored. This yields $\alpha(I,\nu)=\sigma_D N_1^0/(1+I/I'_{\rm op})$. If Γ_{2m} is much larger than Γ_{1v} then $\zeta\simeq 1$ and the expression also simplifies in that case.

*Present address: IBM Research Division, Almaden Research Center, 650 Harry Road, San Jose, CA 95120. Previously associated with the Center for Laser Studies, University of Southern California, University Park, Los Angeles, CA 90089-1112.

†Also at the Center for Laser Studies, University of Southern California, University Park, Los Angeles, CA 90089-1112.

[1]J. Phys. (Paris) Colloq. **7**, C11-83, and references therein; J. E. M. Goldsmith and J. E. Lawler, Contemp. Phys. **22**, 235 (1981).

[2]D. K. Doughty and J. E. Lawler, Appl. Phys. Lett. **45**, 611 (1984); D. K. Doughty, E. A. Den Hartog, and J. E. Lawler, *ibid.* **46**, 352 (1985).

[3]B. N. Ganguly and A. Garscadden, Appl. Phys. Lett. **46**, 540 (1985).

[4]D. M. Pepper, IEEE J. Quantum Electron. **QE-14**, 971 (1978).

[5]M. Maeda, Y. Nomiyama, and Y. Miyazoe Opt. Commun. **39**, 64 (1981); H. B. Valentini, Opt. Commun. **53**, 313 (1985).

[6]J. E. Lawler, Phys. Rev. A **22**, 1025 (1980); D. K. Doughty and J. E. Lawler, *ibid.* **28**, 773 (1983).

[7]M. Jardino, M. Desaintfuscien, and F. Plumelle, J. Phys. Colloq. **8**, C8-327 (1981); J. D. Prestage, G. J. Dick, and L. Maleki, 41st Annual Frequency Control Symposium, Philadelphia, PA, 1987 (unpublished).

[8]J. E. Lawler and A. H. Guenther, Digest of Technical Papers of the 3rd IEEE pulsed power conferences, Albuquerque, New Mexico, 1981 (unpublished), p. 147.

[9]C. Kenty, Phys. Rev. **80**, 95 (1950).

[10]R. B. Winkler, J. Wilhelm, and R. Winkler, Ann. Phys. (Leipzig) **40**, 89 (1983); J. T. Dakin, J. Appl. Phys. **60**, 563 (1986) and references therein.

[11]J. Polman, J. E. van der Werf, and P. C. Drop, J. Phys. D Appl. Phys. **5**, 266 (1972).

[12]L. Vriens, R. A. J. Keijser, and F. A. S. Ligthart, J. Appl. Phys. **49**, 3807 (1978).

[13]J. T. Verdeyen, *Laser Electronics* (Prentice-Hall, Englewood Cliffs, 1981).

[14]C. E. Webb, Inst. Phys. Conf. Ser. **29**, 1 (1976).

[15]N. C. Holmes and A. E. Siegman, J. Appl. Phys. **49**, 3155 (1978); Marc D. Raynor, Ph.D. dissertation, University of Colorado, 1985.

[16]C. Brechignac, R. Vetter, and P. R. Berman, Phys. Rev. A **17**, 1609 (1978).

[17]W. W. Quivers, Jr., Phys. Rev. A **34**, 3822 (1986).

[18]W. Richardson, L. Maleki, and E. Garmire, Opt. Lett. **11**, 572 (1986).

[19]D. R. Lyons, A. L. Schawlow, and G. Y. Yan, Opt. Commun. **38**, 35 (1981).

[20]W. Richardson Ph.D. dissertation, University of Southern California, 1987.

[21]N. A. Kryukov, N. P. Penkin, and T. P. Redko, Opt. Spektrosk. **42**, 17 (1977) [Opt. Spectrosc. (USSR) **42**, 33 (1977)].

[22]F. Reif, *Fundamentals of Statistical and Thermal Physics* (McGraw-Hill, New York 1965), p. 469.

[23]N. Ashcroft and N. Mermin, *Solid State Physics* (Holt, Rinehart and Winston, New York, 1977). The radii are taken as half the nearest neighbor distance.

[24]Chr. Tamm, E. Buhr, and J. Mlynek, Phys. Rev. A **34**, 1977 (1986). The factor 7 is based on a comparison of measurements of the cross section in samarium vapor with results of the hard-sphere collision.

[25]C. Dreze, Y. Demers, and J. N. Gagne, J. Opt. Soc. Am **72**, 912 (1982); R. A. Keller and E. F. Zalewski Appl. Optics **19**, 3301 (1980).

[26]E. Arimondo, M. G. Divito, K. Ernst, and M. Inguscio, Opt. Lett. **9**, 530 (1984).

[27]P. van der Weijer and R. M. M. Cremers, Opt. Commun. **53**, 109 (1985); Opt. Commun. **54**, 273 (1985).

[28]L. Vriens, J. Appl. Phys. **44**, 3980 (1973).

[29]D. M. Kane, J. Appl. Phys. **56**, 1267 (1984).

[30]E. L. Lewis, Phys. Rep. **58**, (1980).

[31]D. G. Steel and R. A. McFarlane, Phys. Rev. A **27**, 1217 (1983).